

Velocity Correlations in Dense Gravity Driven Granular Chute Flow

Oleh Baran, Deniz Ertas, and Thomas C. Halsey
*Corporate Strategic Research, ExxonMobil Research
 and Engineering, Annandale, New Jersey 08801*

Gary S. Grest and Jeremy B. Lechman
Sandia National Laboratories, Albuquerque, New Mexico 87185

(Dated: March 23, 2022)

Abstract

We report numerical results for velocity correlations in dense, gravity-driven granular flow down an inclined plane. For the grains on the surface layer, our results are consistent with experimental measurements reported by Pouliquen. We show that the correlation structure within planes parallel to the surface persists in the bulk. The two-point velocity correlation function exhibits exponential decay for small to intermediate values of the separation between spheres. The correlation lengths identified by exponential fits to the data show nontrivial dependence on the averaging time Δt used to determine grain velocities. We discuss the correlation length dependence on averaging time, incline angle, pile height, depth of the layer, system size and grain stiffness, and relate the results to other length scales associated with the rheology of the system. We find that correlation lengths are typically quite small, of the order of a particle diameter, and increase approximately logarithmically with a minimum pile height for which flow is possible, h_{stop} , contrary to the theoretical expectation of a proportional relationship between the two length scales.

I. INTRODUCTION

Dense, gravity-driven granular flows down an inclined plane [1, 2, 3, 4] achieved the status of a key model system because of their relevance to many geological and industrial applications. Provided that the surface of the incline is sufficiently rough and the flow height is small compared to the width and length of the chute, such that transients and side-wall effects can be neglected, the flow behavior is controlled by the angle of inclination, θ , and granular layer thickness h . For a given θ the flow is possible only for $h > h_{\text{stop}}(\theta)$. Here h_{stop} is often referred to as the deposit function, because it is approximately equal to the thickness of the deposit remaining on the plane once the flow is stopped either due to the decrease of θ or decrease of h . Recent experimental and numerical studies confirmed that for spherical grains, the depth-averaged steady state velocity of the flow u can be related to the deposit function through the following relationship, originally proposed by Pouliquen [2, 5]:

$$\frac{u}{\sqrt{gh}} = \beta \frac{h}{h_{\text{stop}}(\theta)}, \quad (1)$$

where g is the gravitational acceleration and $\beta \approx 0.13$. This relationship suggests that a single scaling length controls both the deposit function and the rheology.

A potential explanation of this scaling length as arising from correlations in granular motion was advanced by some of us [6], linking a correlation length in the flow to a rheologically defined “viscosity length scale”, l_ν , defined by the Bagnold scaling form [6]

$$\sigma_{xz} = \rho l_\nu^2 \dot{\gamma}^2, \quad (2)$$

for a granular system with bulk density ρ , flowing under a shear stress σ_{xz} at a shear rate $\dot{\gamma}$. Alternatively, it has recently been argued [7, 8] that for a granular system made of particles of diameter d and grain density ρ_g flowing while subject to a pressure P , the rheology is controlled by the local scaling variable

$$I = \frac{\dot{\gamma}d}{\sqrt{P/\rho_g}}, \quad (3)$$

which is a generalization of Eq.(1). For steady state chute flow, these two quantities are related through

$$I = \frac{d}{l_\nu} \sqrt{\frac{\tan \theta}{\phi}}, \quad (4)$$

where ϕ is the volume fraction, thus they can be used interchangeably in this case. The fact that the same rheology can be advanced with or without an assumed fundamental length scale (a “correlation length”) raises questions about the correct interpretation of this length scale, and the nature of its relationship to flow-induced structures, if any. Pouliquen [9] has recently reported experimental measurements of two point velocity correlation functions at the flow surface, and obtained results supporting a possible connection between the observed correlation length and the deposit function.

In this work, we repeat and extend the correlation analysis presented by Pouliquen [9] to layers that are far from the bottom and surface of the flow, where true bulk rheology is observed, by taking advantage of information available from discrete element (DEM) simulations that is difficult to obtain experimentally. We are able to reproduce and further analyze the experimental results, and ultimately make the following observations:

- All two-point velocity correlation functions exhibit exponential decay with relative distance, generally with different values of the correlation length $\lambda_{\alpha\beta}$ for different components β of the velocity and α of the displacement vector.
- The measured correlation lengths $\lambda_{\alpha\beta}$ vary with the velocity measurement time Δt used to calculate the velocities from displacements. In order to be able to compare correlation lengths at different depths and between different runs, it is necessary to adjust the measurement time such that the particles that are being measured experience a fixed, predetermined strain $\epsilon = \dot{\gamma}\Delta t$. This yields correlation lengths that are independent of the position of the measured layer in the bulk, or the overall flow height.
- Correlation lengths in the bulk are uniquely determined by the incline angle θ (or equivalently by h_{stop} or I). They increase with decreasing θ .
- Correlation lengths are typically quite small, of the order of a particle diameter, and increase approximately logarithmically with h_{stop} , contrary to the theoretical expectation of a proportional relationship between the two length scales.
- For very high piles and angles close to the angle of repose, the flows excite a low frequency “breathing mode” with coherent motion normal to the surface layer, previously

observed by Silbert [10]. This limits our ability to probe the limit of large h_{stop} , small I in this geometry.

The paper is organized as follows: In Section II we outline the simulation method, which has been described in detail elsewhere [2], and explain the analysis used to obtain the reported results. In Section III A we present the results of velocity correlations analysis in the surface layer and compare these results with those of Pouliquen [9]. In Section III B we discuss the differences between correlations on the surface and in the bulk. We then report the results for velocity correlations in the bulk in Section III C. We also discuss the velocity fluctuations in Appendix A and the effect of system size and stiffness of particles on the correlation length in Appendix B. Finally, in Section IV we present our conclusions.

II. SIMULATION AND ANALYSIS METHOD

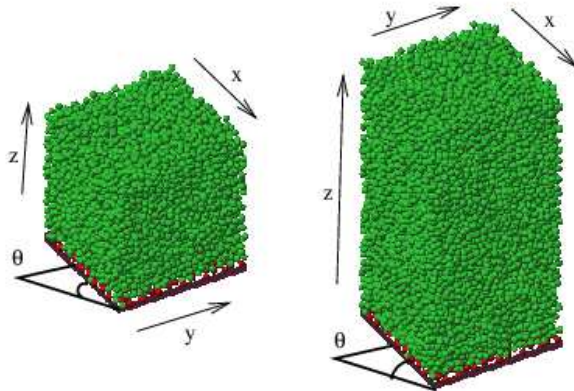


FIG. 1: (Color online) Typical snapshots from simulations with labeled coordinate axes. θ is an angle of inclination of the rough base. Base area $20d \times 20d$. 9089 spheres in the system of height $h/d \simeq 20$ (left) and 17889 spheres in the system of height $h/d \simeq 40$ (right).

A. Simulation Method

We perform three-dimensional discrete element (DEM) simulations of spherical, monodisperse particles of diameter d in the chute flow geometry. The simulation method is described in detail in Ref. [2]. The simulation cell consists of a rough bottom in the xy -plane, whose

normal is tilted by an angle θ with respect to the direction of gravitational acceleration g in order to induce a flow in the x -direction, as shown in Fig. 1. The bottom is roughened by a thin substrate of stationary particles uniformly distributed over the base of the system with the same properties as the mobile particles. Periodic boundary conditions are imposed in x - and y - directions with a typical base size of $20d \times 20d$, in order to eliminate the documented effect of side walls [11].

The mobile particles flowing above the base are spheres of mass m and diameter d that form Hertzian contacts as well as interacting frictionally. Unless otherwise noted, the simulation parameters used for the runs were $k_n = 2 \times 10^5 mg/d$ (normal contact stiffness), $\mu = 0.5$ (Coulomb friction coefficient), $k_t = (2/7)k_n$ (tangential contact stiffness), $\gamma_n = 50 \sqrt{g/d}$ (normal viscoelastic constant) and $\gamma_t = 0$ (tangential viscoelastic constant) [15]. In Appendix B we also present results with reduced ($k_n = 2 \times 10^3 mg/d$) and increased ($k_n = 2 \times 10^7 mg/d$) stiffness of particles.

We evolve the system by integrating the appropriate equations of motion [2] with a timestep $\delta t/\tau_0 = 10^{-4}$, where the characteristic time $\tau_0 = \sqrt{d/g}$. In order to ensure measurements in steady state, we equilibrate each system for a long enough time ($1 - 2 \times 10^7 \delta t$) and check the stationarity of velocity profiles. Our main comparative analysis is applied to simulations with a base area of $20d \times 20d$ with two different flow heights ($h/d \simeq 20$ with 9089 particles and 40 with 17889 particles) at different angles θ in the range between 20.5° and 26° .

The main properties of the runs with typical parameters, as well as the results of the correlation analysis for the selected layers in the bulk of these flows, are summarized in Table I. The steady-state volume fraction and velocity profiles of these runs are depicted in Fig. 2. In addition, we simulated and obtained selective results for thin piles, $h/d \simeq 10$, with typical ($20d \times 20d$) and large ($40d \times 40d$) base area (see Appendix B) as well as taller piles, $h/d \simeq 80$.

B. Velocity Correlation Analysis Method

All correlation analyses are performed at steady state, within thin layers normal to the z -axis. The surface correlation analysis was applied to a preset number of particles ($N_{\text{layer}} = 400$ for the typical bases size of $20d \times 20d$, to obtain approximately one layer of particles) with

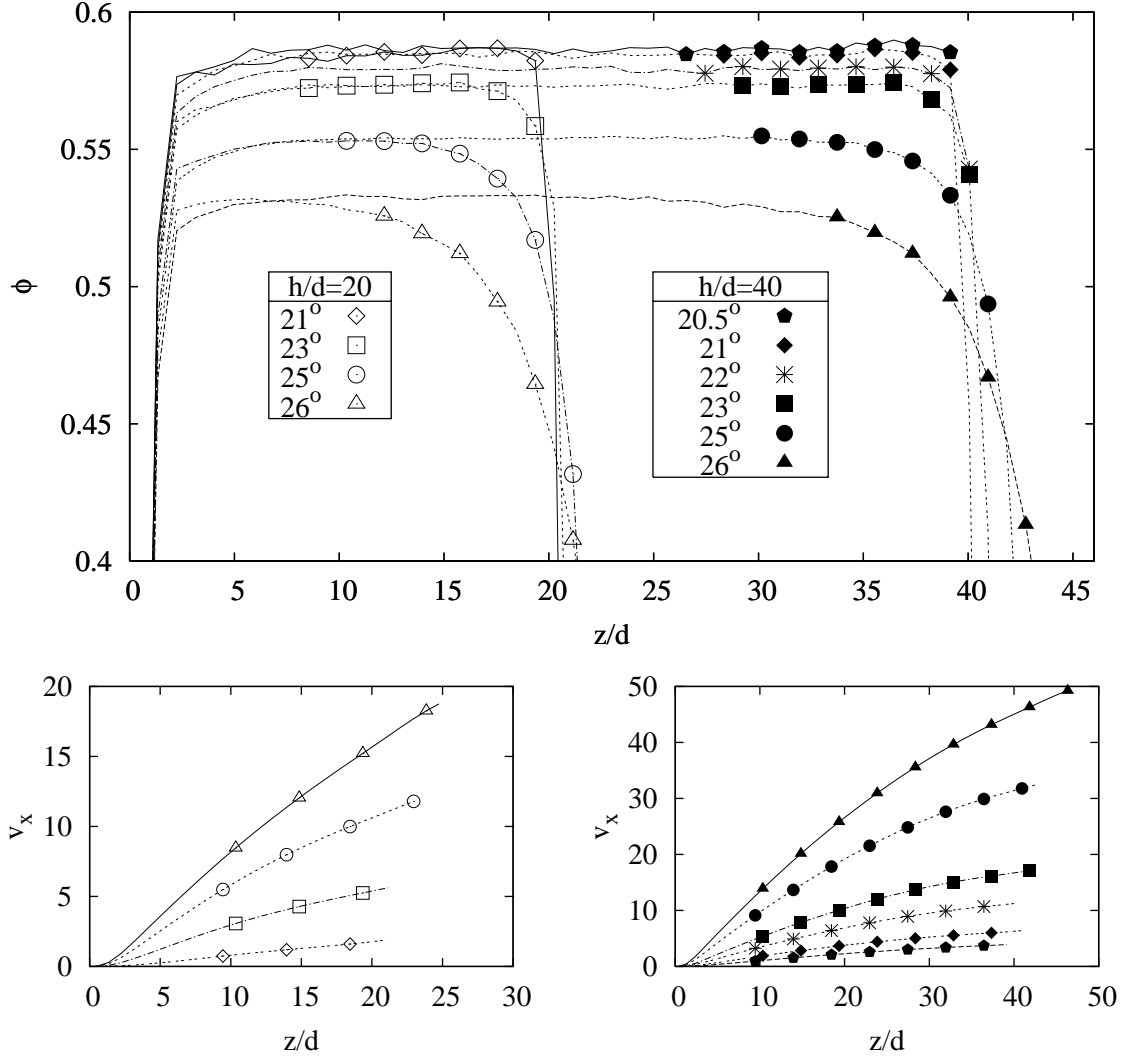


FIG. 2: (a) Volume fraction profiles for all systems listed in Table I. (b) Velocity profiles for $h/d \simeq 20$. (c) Velocity profiles for $h/d \simeq 40$. See also Table I for legend information. All profiles are obtained with bin size of $0.9d$. All data points are connected with lines and the symbols are used to mark each data-set.

the largest z -values. Bulk layers that were analyzed included all particles whose centers were located within $0.5d$ of the plane located at $z = z_{\text{layer}}$. This yielded $N_{\text{layer}} \approx 400 - 440$ particles in the layer, depending on θ . The results are not sensitive to variations of N_{layer} or bulk layer thickness by 10 – 15%.

The values for z_{layer} , reported in Table I, are chosen near the center of the pile, in order to minimize boundary effects from the top and bottom. In order to ensure that bulk properties are observed in these layers, in Fig. 3 we display the scaling variable I [cf. Eq.(3)] as a




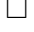





θ	20.5°	21°	21°	22°	23°	23°	25°	25°	26°	26°
$h_{\text{stop}}/d^\dagger$	19.6	16.4	16.4	12.1	9.0	9.0	5.0	5.0	3.6	3.6
h/d	40	20	40	40	20	40	20	40	20	40
Legend				*						
ϕ_{bulk}	.586	.584	.584	.578	.573	.572	.553	.554	.526	.532
$z_{\text{layer}}/d^\ddagger$	25.0	11.5	25.0	25.0	11.5	25.0	11.5	25.0	11.5	25.0
$\langle v_x \rangle$	2.79	.95	4.57	8.32	3.40	12.46	6.68	23.09	9.42	32.17
$\dot{\gamma}\tau_0$.096	.101	.144	.258	.286	.390	.556	.730	.820	1.053
I	.025	.034	.038	.067	.096	.101	.182	.183	.259	.253
$\langle (u_x^{\text{inst}})^2 \rangle$.018	.014	.026	.060	.060	.109	.186	.314	.395	.639
$\langle (u_y^{\text{inst}})^2 \rangle$.011	.010	.020	.046	.046	.084	.139	.234	.296	.471
$\langle (u_z^{\text{inst}})^2 \rangle$.019	.012	.026	.055	.055	.098	.162	.272	.338	.539
$\lambda_{yy}^{\epsilon=0.1}/d$	1.36	1.40	1.34	1.24	1.18	1.17	1.02	1.00	0.84	0.86

TABLE I: Properties of the simulation runs and associated bulk layers that were analyzed for velocity correlations.

\dagger : From Ref. [12]: The tangential viscoelastic constant $\gamma_t = \gamma_n/2$. However, h_{stop} is not affected by this difference.

\ddagger : Layer thickness is one diameter, centered around the reported z_{layer} .

function of z -position, along with the position of the layers for which detailed analysis is conducted. I is expected to be constant in the bulk [7].

In the PIV technique used in laboratory experiments, velocities are obtained by measuring particle displacements between two frames separated by the time Δt . Similarly, we measure the velocity of each particle $i \in \{1..N_{\text{layer}}\}$ in a layer from its displacement over a characteristic “measurement time” Δt :

$$v_\alpha^i(t) = (r_\alpha(t) - r_\alpha^i(t - \Delta t)) / \Delta t. \quad (5)$$

Here $\alpha = \{x, y, z\}$ is a coordinate label and $\mathbf{r}^i(t)$ is the position of particle i at time t .

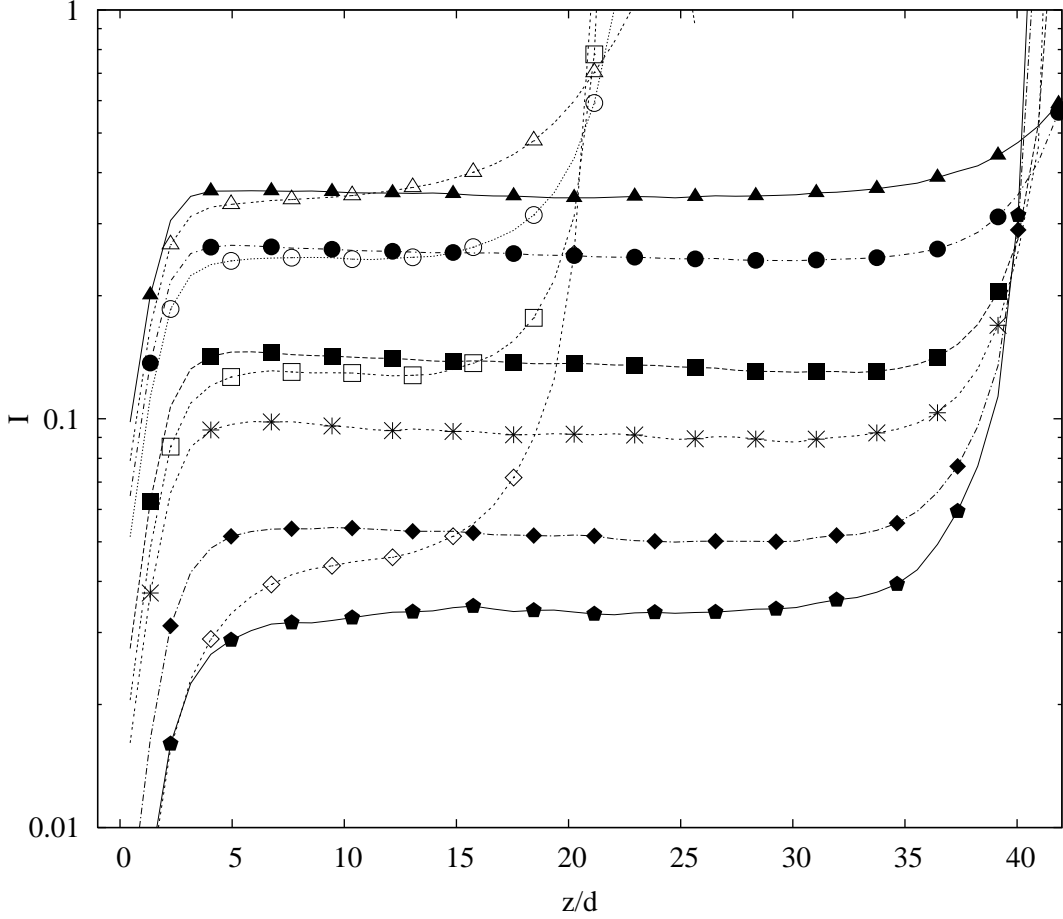


FIG. 3: Scaling variable I versus scaled height z/d .

Due to finite size effects, the instantaneous mean velocity of each layer,

$$\bar{v}_\alpha(t) = \sum_i^{N_{\text{layer}}} v_\alpha^i(t) / N_{\text{layer}}, \quad (6)$$

fluctuates around the time-averaged velocity profile shown in Fig. 2(b-c). In order to avoid introducing spurious correlation effects at large distances, we use the instantaneous mean velocity to obtain the velocity fluctuations, rather than the long-time mean velocity:

$$u_\alpha^i(t) = v_\alpha^i(t) - \bar{v}_\alpha(t). \quad (7)$$

Finally, to obtain better statistics, we perform the correlation analysis for $N_T \approx 10^4$ configurations separated by $100 \delta t$. Although not explicitly indicated, all velocities v_α^i have an implicit dependence on the measurement time Δt .

We compute six two-point velocity correlation functions in the xy -plane for each layer, following the method in Ref. [9]. Correlations in the $\beta = \{x, y, z\}$ component of the velocity

at a distance r along the $\alpha = \{x, y\}$ direction are given by

$$C_{\alpha\beta}(r) = \frac{\sum_t [\sum_{i,j} u_\beta^i u_\beta^j \prod_{\gamma=\{x,y\}} \delta(r_\gamma^i - r_\gamma^j + \delta_{\gamma\alpha} r)]}{\sum_t [\sum_{i,j} \prod_{\gamma=x,y} \delta(r_\gamma^i - r_\gamma^j + \delta_{\gamma\alpha} r)]}. \quad (8)$$

Here $\delta(r) = \frac{1}{\sqrt{2\pi}w} \exp(-\frac{r^2}{2w^2})$ is a Gaussian function of width $w = 0.4d$, as used in Ref. [9], and $\delta_{\gamma\alpha} = 1$ when $\gamma = \alpha$ and 0 otherwise. We do not examine correlations along the z -direction since these connect particles with different average velocities and strain rates, which could not be statistically averaged in a satisfactory manner.

In virtually all cases, a good fit to an exponential decay is obtained. Nonexponential behavior was typically related to finite-size effects, poor statistics or dispersion effects, which will be discussed in Section III A. A correlation length $\lambda_{\alpha\beta}$ is associated with each correlation function by obtaining the best linear fit to a log-linear plot:

$$C_{\alpha\beta}(r) = C_{\alpha\beta}(0) \exp(-r/\lambda_{\alpha\beta}). \quad (9)$$

Note that Pouliquen [9] defined the correlation length as the distance $L_{\alpha\beta}$ for which $C_{\alpha\beta}(r) = 0.07C_{\alpha\beta}(0)$, which is related to our correlation length through

$$L_{\alpha\beta} \approx 2.66\lambda_{\alpha\beta}. \quad (10)$$

III. RESULTS

A. Velocity Correlations at the Surface

Figure 4 shows sample vector plots of the velocity field $\mathbf{u}^i(t)$, projected on the xy -plane, with $\Delta t/\tau_0 = 1$, for the surface layers of two simulation runs with $h/d \simeq 20$ and incline angle $\theta = 21^\circ$ and $\theta = 23^\circ$ respectively. Visual inspection of the patterns suggest more correlated flow structures for the lower angle run, similar to observations made in Ref. [9].

For a more quantitative analysis of the velocity correlations, in Fig. 5 we show all six normalized correlation functions (cf. preceding Section) for the pair of runs discussed above. From the linear decrease of $\log[C_{\alpha\beta}(r)]$ with distance, we can determine a correlation length with each normalized correlation function by fitting to Eq.(9).

It is instructive to compare the profiles in Fig. 5 to those in Fig. 6, which are obtained from exactly the same data set, but by using the time-averaged mean velocity instead of the

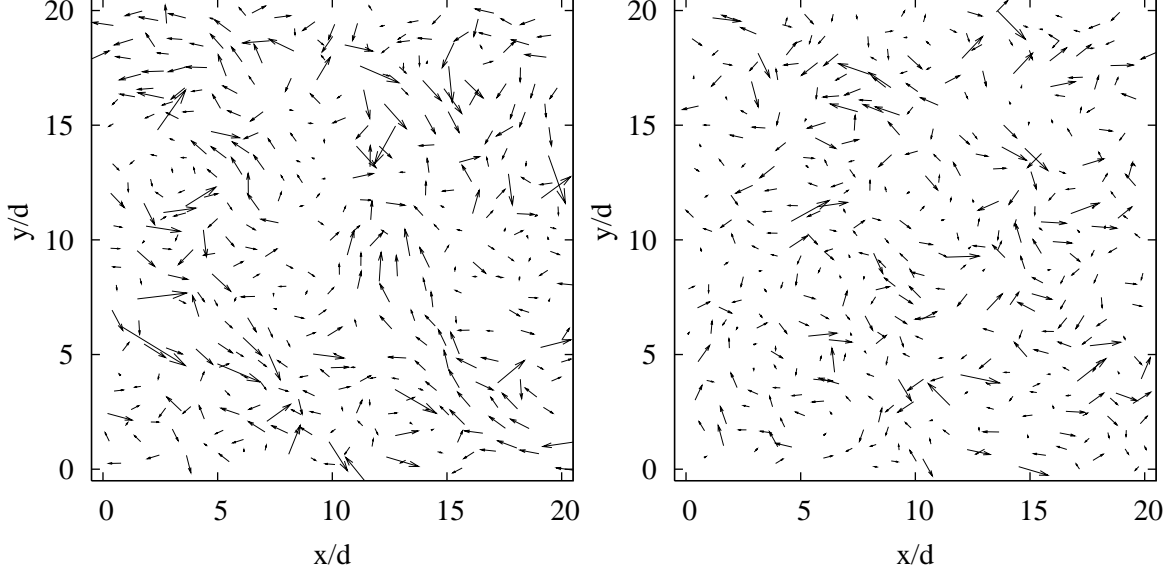


FIG. 4: Sample velocity fields in the xy -plane for the surface layers of two runs with $h/d \simeq 20$ and $\Delta t/\tau_0 = 1$. (a) $\theta = 21^\circ$, (b) $\theta = 23^\circ$.

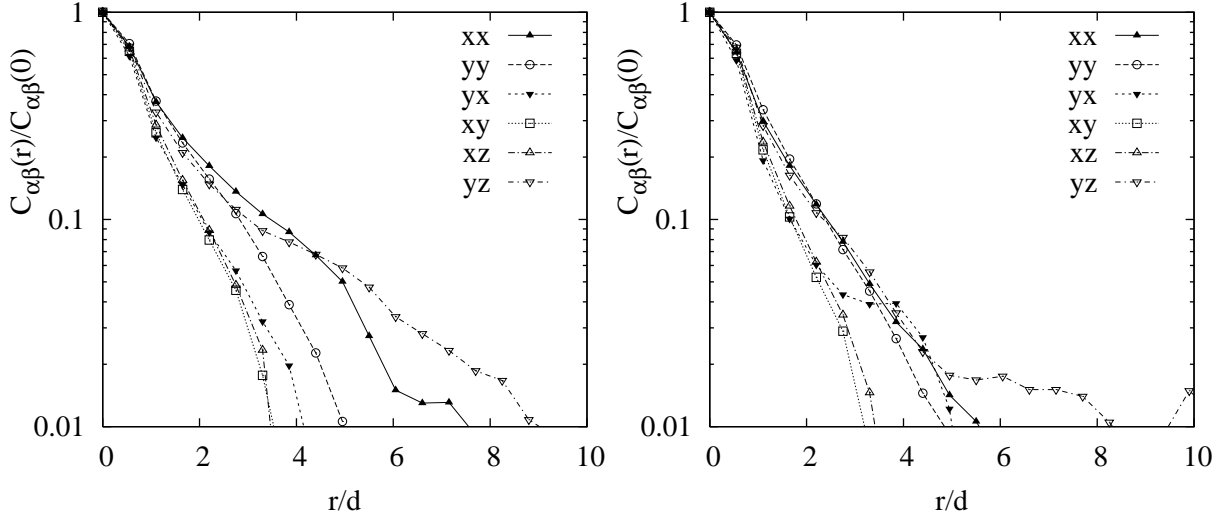


FIG. 5: The six normalized correlation functions, $C_{\alpha\beta}(r)$, for two runs with $h/d \simeq 20$ and $\Delta t/\tau_0 = 1$. (a) $\theta = 21^\circ$ and (b) $\theta = 23^\circ$.

instantaneous mean velocity to compute velocity fluctuations. Effectively, this corresponds to switching the order of spatial averaging and temporal averaging and is not expected to affect the result in a large system in steady-state. However, spurious correlations are obtained when the latter method is used, which are due to the fluctuations in the instantaneous mean velocity shown in Fig. 7. The largest deviations in Fig. 6(a) arise for $C_{\alpha x}(r)$, consistent

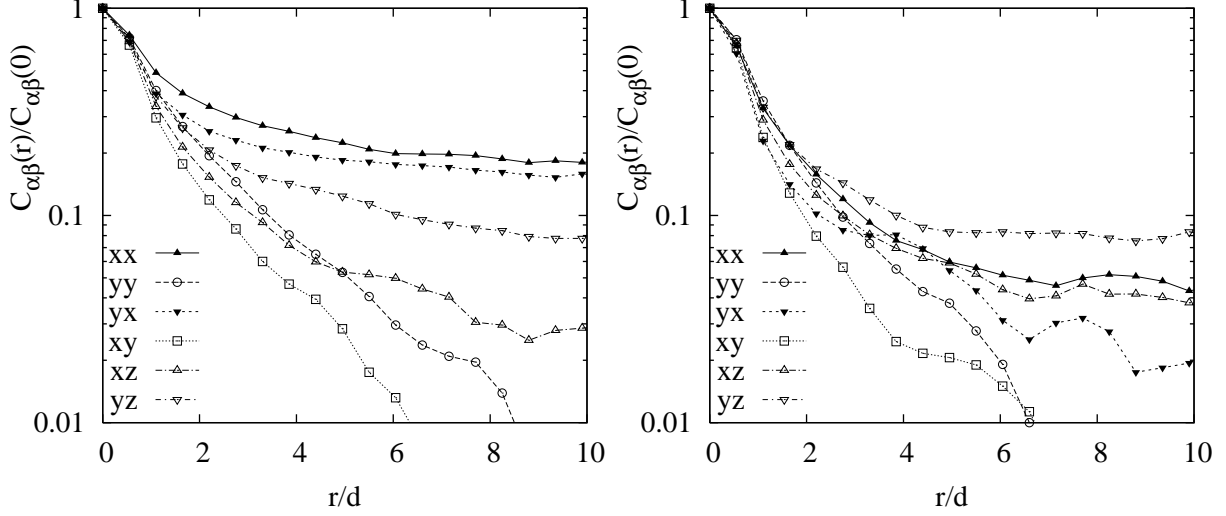


FIG. 6: The six normalized correlation functions, for the same runs shown in Fig 5, but with relative velocities computed by subtracting the time-averaged mean velocity instead of the instantaneous mean velocity. Note the “flattening” of the correlation functions at large distances (see text).

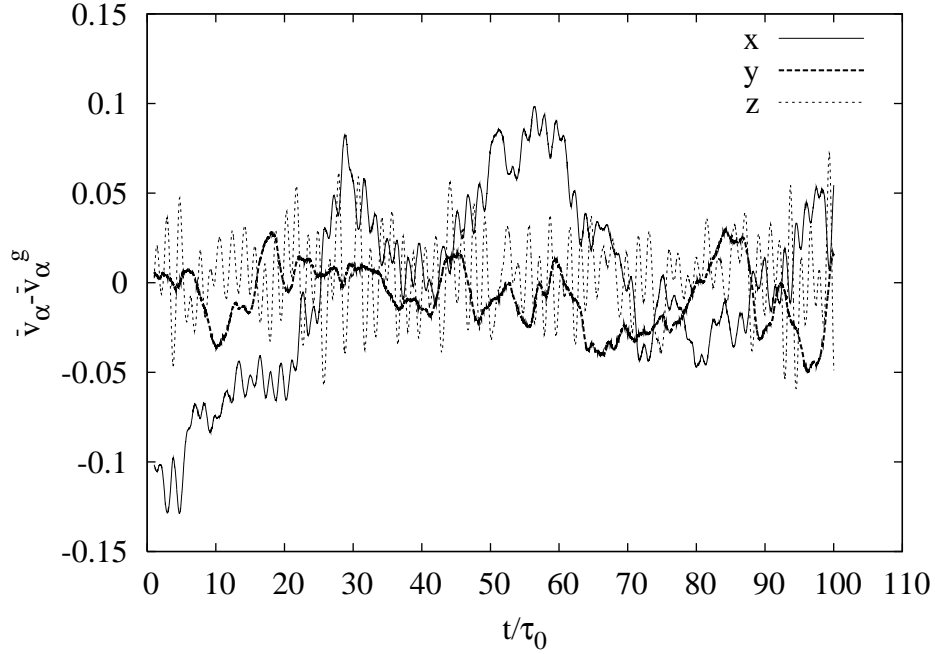


FIG. 7: Fluctuating components of surface layer velocity for $h/d \simeq 20$, $\theta = 21^\circ$.

with the largest deviations in $\bar{v}_x(t)$ seen in Fig. 7. The resemblance of these to some of the correlation functions shown in Ref. [9], which uses the global mean velocity, suggests that

the combination of the observed non-exponential tails and the particular definition of the correlation length $L_{\alpha\beta}$ used may have resulted in over-estimation of the reported correlation lengths. We typically obtain the least systematic bias in the y -component of the velocity and therefore rely mainly on $C_{yy}(r)$ for comparative analysis of runs.

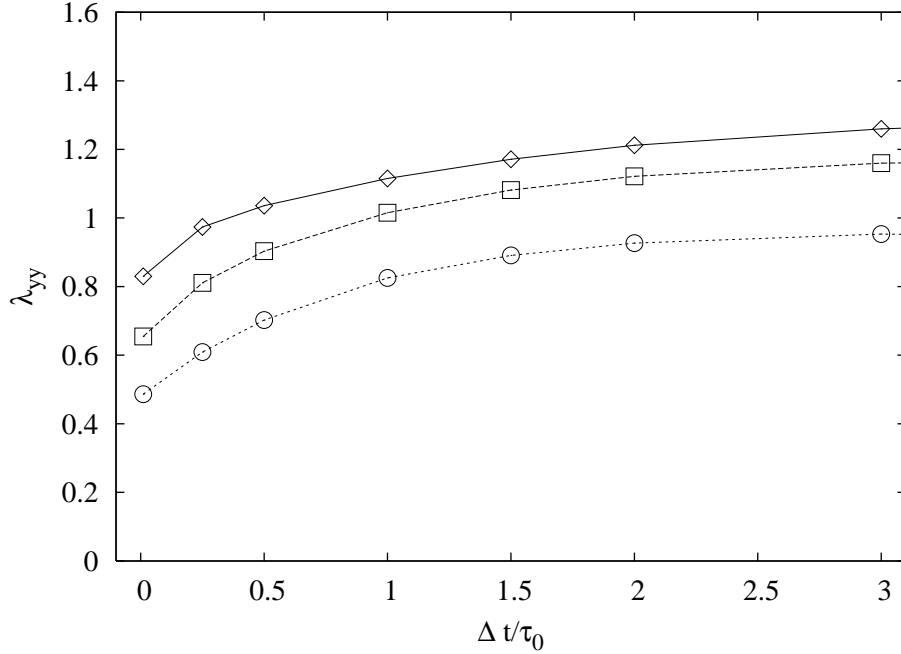


FIG. 8: Surface layer correlation length as a function of Δt for $h/d \simeq 20$ and $\theta = 21^\circ$ (\diamond), $\theta = 23^\circ$ (\square) and $\theta = 25^\circ$ (\circ).

Although we confirm that the measured correlation is indeed larger for the smaller angle run, we find that the velocity correlation lengths depend on the measurement time, Δt . As seen in Fig. 8, the correlation length initially increases with Δt , ultimately reaching a maximum value as the mean strain experienced by the particles during the measurement time, $\epsilon \equiv \dot{\gamma}\Delta t$, exceeds 1. The plateau at large Δt is understandable: The velocity correlations are naturally disappearing as particles start to execute diffusive motion induced by the strain. However, the initial increase in λ_{yy} makes it difficult to decide the “correct” measurement time to use in order to appropriately compare runs with different heights and angles. We discuss this issue in more detail in Appendix A and arrive at the conclusion that the results should be compared at the fixed values of measurement strain $\epsilon = \dot{\gamma}\Delta t$.

B. Depth dependence of velocity correlations

Since our main interest is in the nature of granular flow in the bulk, we next investigate how the velocity correlation length varies as a function of distance from the surface by taking advantage of the information available in simulations but usually not in experiments.

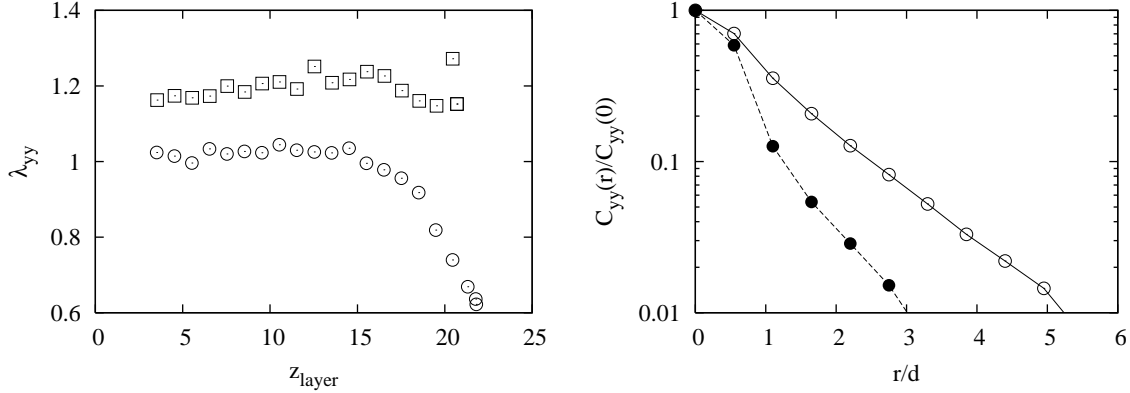


FIG. 9: (a) Correlation length λ_{yy} profiles for angles 23° (squares) and 25° (circles), height $h/d \simeq 20$. (b) $C_{yy}(r)$ at the surface (filled circles) and in the bulk (open circles) for $\theta = 25^\circ$ and $h/d \simeq 20$. All results are obtained for fixed strain $\epsilon = 0.1$.

Figure 9(a) shows the correlation length profiles as a function of interrogated layer position z_{layer} for $h/d \simeq 20$ and angles 23° and 25° . The correlation length is slightly smaller near the top of the pile compared to the bulk, where it is approximately constant. The correlation lengths increase as the angle is decreased towards the angle of repose. This is consistent with earlier observations reported on surface correlations [9].

Figure 9(b) shows typical shapes of correlation functions for $h/d \simeq 20$, $\theta = 25^\circ$, $\epsilon = 0.1$ in the bulk compared to the surface. $C_{yy}(r)$ on the surface has more noise than in the bulk, which is most probably due to the saltating particles. Fluctuations in the mean velocity are dominated by a relatively small number of saltating particles at the surface. Since such particles do not exist in the bulk layers, the statistics is better in the bulk layers. Furthermore, the rheology of chute flow becomes more robust and better characterized in the bulk. Therefore, in order to make a more quantitative connection between the correlation length λ_{yy} and deposit function $h_{\text{stop}}(\theta)$, we will focus on the bulk flow for the remainder of this paper.

C. Correlations in the bulk

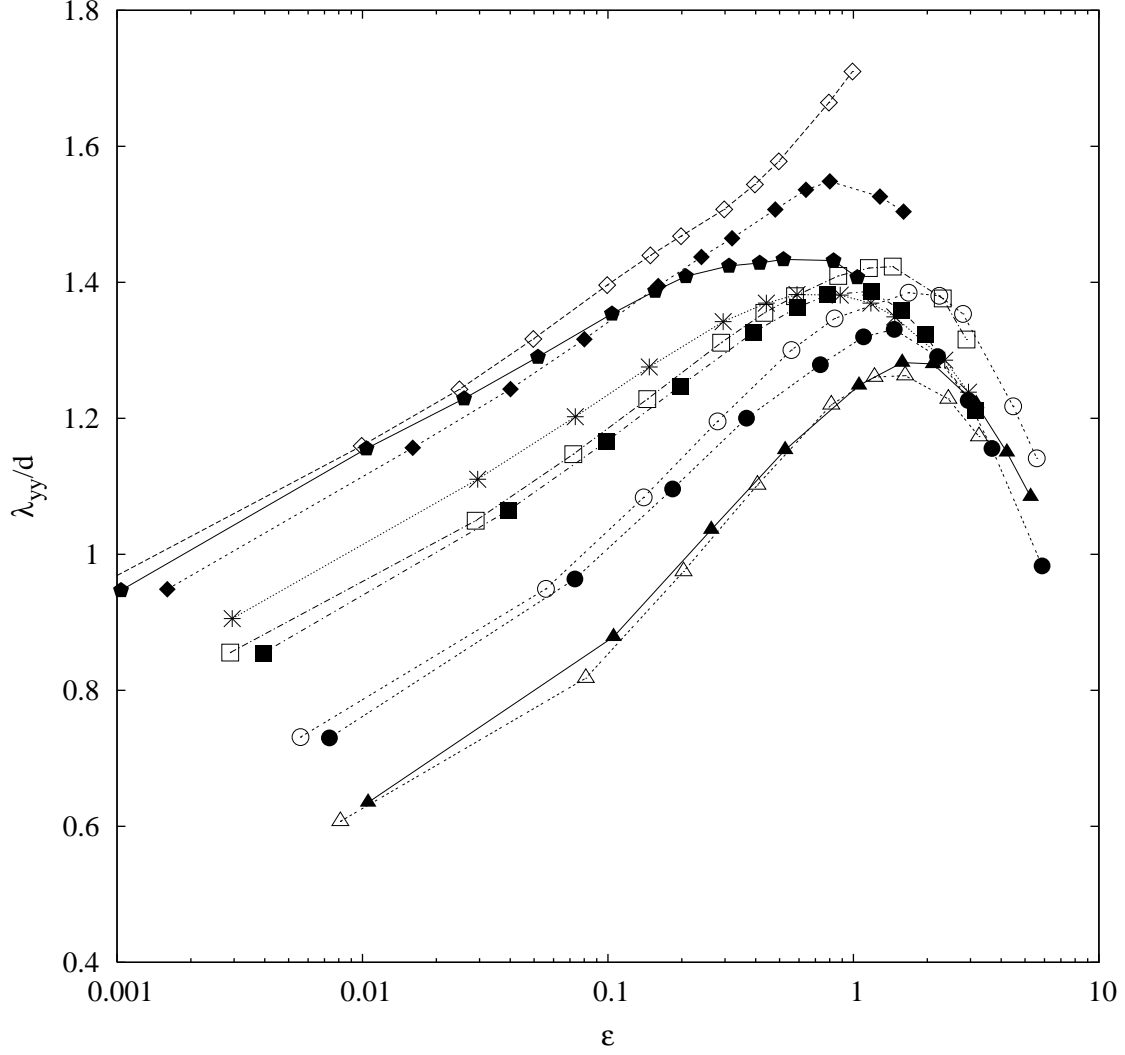


FIG. 10: Correlation length λ_{yy} as a function of strain.

Figure 10 shows the correlation length λ_{yy} as a function of ϵ , for all the runs described in Table I. As discussed in Section III A, the comparison of correlation lengths at different angles should be done at a fixed value of ϵ , for which the rattling motion has largely averaged away and decorrelation due to the diffusive motion has not yet set in. For the systems listed in Table I, the region $0.1 < \epsilon < 0.2$ is the most suitable.

In Fig. 11(a), λ_{yy} , measured at $\epsilon = 0.1$ as a function of I , is displayed. The dependence is quite weak, and λ_{yy} appears to diverge only logarithmically, if at all, in the $I \rightarrow 0$ limit. In contrast, h_{stop} exhibits stronger dependence and power-law divergence in the same

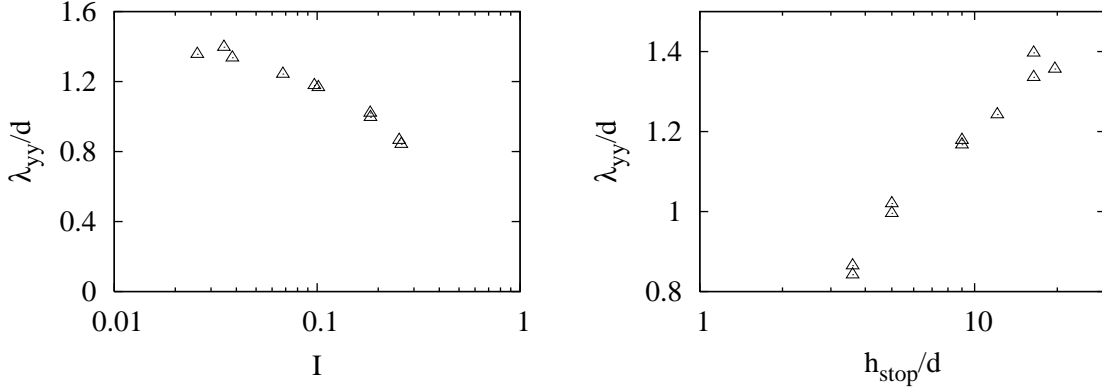


FIG. 11: (a) λ_{yy} versus I and (b) λ_{yy} versus h_{stop} for $\epsilon = 0.1$.

limit. The interdependence of λ_{yy} and h_{stop} is directly probed in Fig. 11(b), which reveals an approximate relationship $\lambda_{yy}/d \sim \ln(h_{\text{stop}}/d)$. This result suggests that the velocity correlation length remains much smaller than the pile height for all flowing piles in the $I \rightarrow 0$ limit and does not directly influence h_{stop} . In fact, the situation appears to bear an interesting similarity to that in molecular glasses, where the diverging viscosity at the glass transition is accompanied by a region of cooperative motion that remains quite small and appears to show signs of a logarithmic divergence [13].

To probe smaller values of I one needs to study thick piles at low angles just above the angle of repose. However, it has recently been shown by Silbert [10] that these flows exhibit flow instabilities. For example, for $(h \simeq 80)$ and $\theta \leq 21^\circ$, a resonant normal vibration mode is present which results in a longitudinal dilation wave in the z -direction. As a result, the density in a given layer, as well as the height of the flow, varies periodically in time, breaking the time-translation symmetry.

IV. CONCLUSIONS

We have presented numerical evidence that the spatial correlations associated with velocity fluctuations in chute flow decay exponentially with distance and remain short-ranged, with the correlation lengths exhibiting at best a logarithmic divergence as the angle of repose is approached. In order to make meaningful comparisons of correlation lengths, it is important to choose measurement times that are inversely proportional to the local strain rate. As described in Appendix A, the analysis of single particle motion reveals two su-

perimposed motions: Cage rattling that dominates the instantaneous velocity fluctuations but lacks correlation and sterically constrained motion that causes strain-induced diffusion and reflects correlations in particle rearrangement. A closed-form set of rheological equations would need to relate hydrodynamic flow parameters to the microscopic energy dissipation in the system, and unraveling this relationship would likely need to take into account the quite different dissipation characteristics of these two types of motions.

Acknowledgments

Sandia is a multiprogram laboratory operated by Sandia Corporation, a Lockheed Martin Company, for the United States Department of Energy's National Nuclear Security Administration under Contract No. DE-AC04-94AL85000.

APPENDIX A: DEPENDENCE ON EFFECTIVE STRAIN

The velocity correlation results depend on measurement time, Δt , and measurement strain $\epsilon = \dot{\gamma}\Delta t$. We found it instructive to study the distribution of velocity fluctuations as a function of measurement strain $\epsilon = \dot{\gamma}\Delta t$. To avoid the effects of boundaries we show here the results for bulk layers listed in Table I. Figure 12 depicts non-dimensionalized mean square velocity fluctuations as a function of ϵ :

$$\sigma_{\alpha}^2(\epsilon) \equiv \frac{\langle u_{\alpha}^2 \rangle}{(\dot{\gamma}d)^2}, \quad (\text{A1})$$

where u_{α} is obtained using a measurement time $\Delta t = \epsilon/\dot{\gamma}$.

The inset in the figure shows that a simple Gaussian distribution is observed in all cases, such that the variance completely characterizes the fluctuations. For an individual data set, we observe a ballistic-like regime for small ϵ , in which the measured velocities do not depend on ϵ , whereas particles exhibit diffusive motion at larger values of ϵ .

The collapse of all data for large ϵ suggests that the diffusive motion at long times is dictated by steric constraints between particles as they pass near each other, such that the displacement of each particle depends only on accumulated strain and not the strain rate. Hence, the velocity fluctuations arising from this motion do not depend on the scaling variable I .

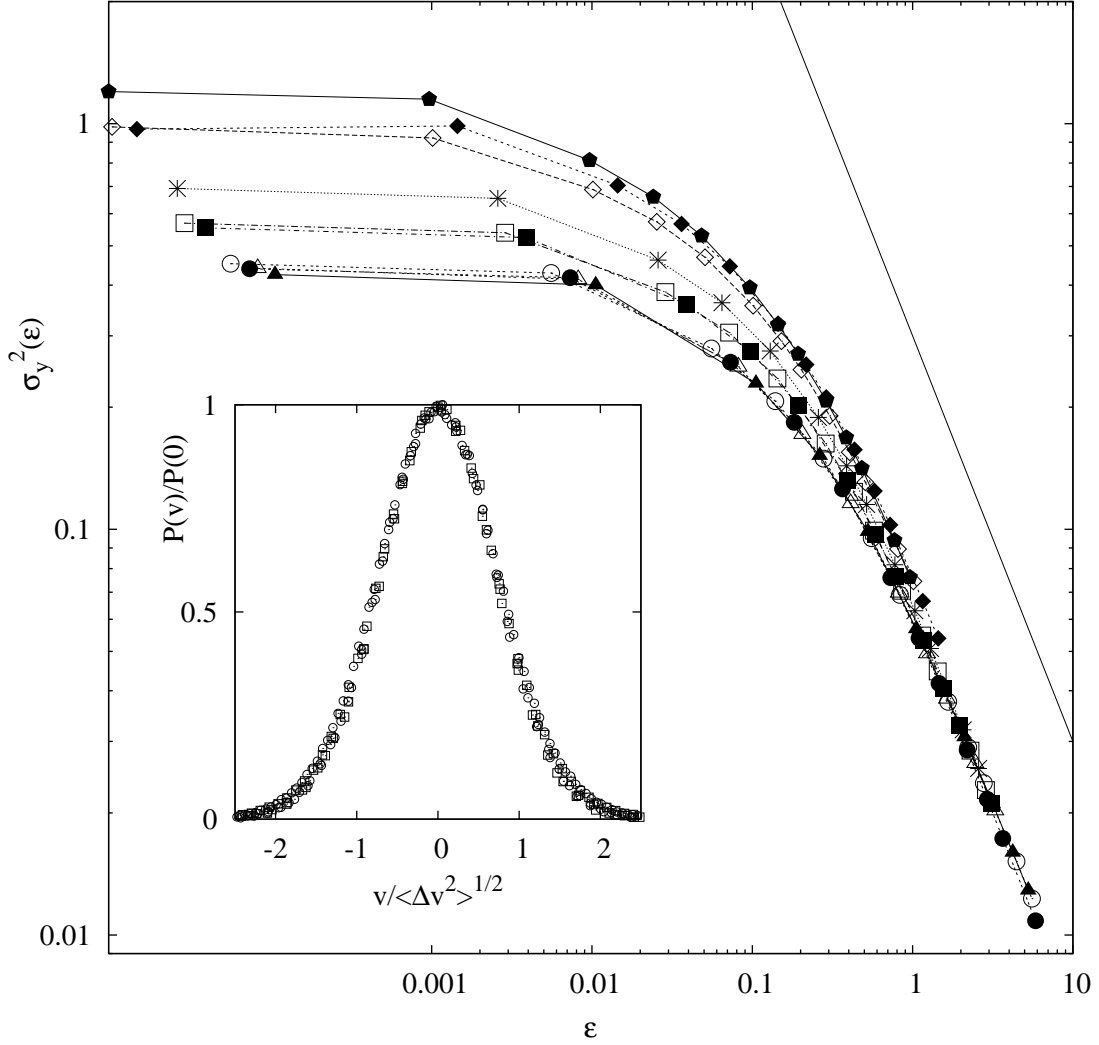


FIG. 12: y -component of the mean square velocity fluctuations versus strain, measured in bulk layers as characterized in Table I. Legend is shown in Table I. Inset shows the probability distribution functions for the y -velocity component in the bulk layer for different runs and Δt 's for $h/d \simeq 20$. The probability is scaled by maximum value and velocities scaled by variance.

In the ballistic-like regime the data-sets diverge from each other. In particular, the instantaneous velocity fluctuations for small ϵ exhibit anomalous scaling $\sigma_\alpha^2(0) \sim I^{-1}$ in the limit $I \rightarrow 0$, as shown in Fig. 13 and observed previously [7]. We associate this additional motion at short times with the rattling of particles in their temporary cages. A more quantitative description of this superimposed grain motion will be discussed elsewhere [14]. This motion is expected to have very weak spatial correlation and average out quickly with increasing measurement time, while still dominating the instantaneous velocity fluctuations

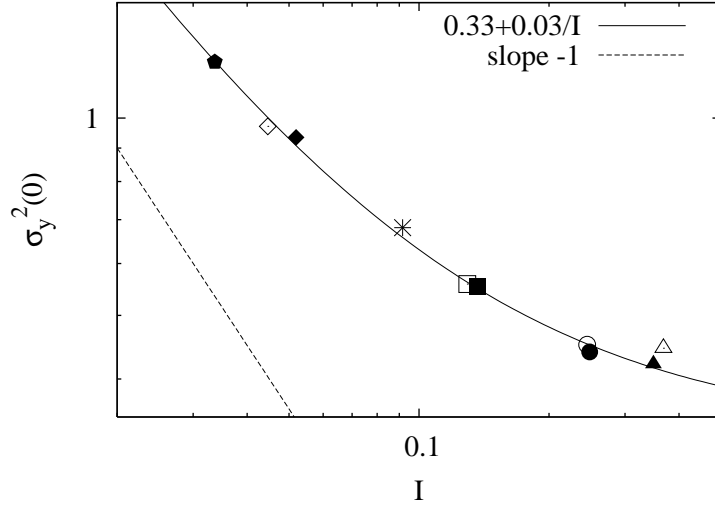


FIG. 13: Velocity fluctuations versus inertial number I for the systems listed in Table I.

and giving rise to their anomalous scaling. Since the overall motion of each particle is the superposition of these two motions, it is not surprising that the measured correlation length is suppressed at small measurement times. Since we are interested in identifying the nature of correlations associated with the sterically hindered motion of the particles, we compare correlation lengths for different systems at a fixed value of measurement strain that is large enough to have substantially eliminated the effects of cage motion, but small enough that the diffusive motion has not caused substantial decorrelation. Note that this effectively changes the measurement time that must be used to determine velocities according to the local strain rate.

APPENDIX B: EFFECT OF SYSTEM SIZE AND PARTICLE'S STIFFNESS

To test the system size effect on the correlation length we equilibrated additional configurations of height $h/d \simeq 10$ at $\theta = 23^\circ$ with two sizes of base area, $20d \times 20d$ and $40d \times 40d$.

Figure 14(a) shows that the volume fraction profiles for the system with base area $40d \times 40d$ is the same as for typical configurations whose bases are $20d \times 20d$. Figure 14(b) shows the velocity correlation functions for the large system compared with the small system size. The correlation lengths, obtained from the exponential fit to the first four points, are very similar, $L_{yy}(40 \times 40) = 1.295$, $L_{yy}(20 \times 20) = 1.240$, $L_{xx}(40 \times 40) = 1.194$, $L_{xx}(20 \times 20) = 1.141$, (less than 5% difference). The deviation in exponential behavior in the smaller system is

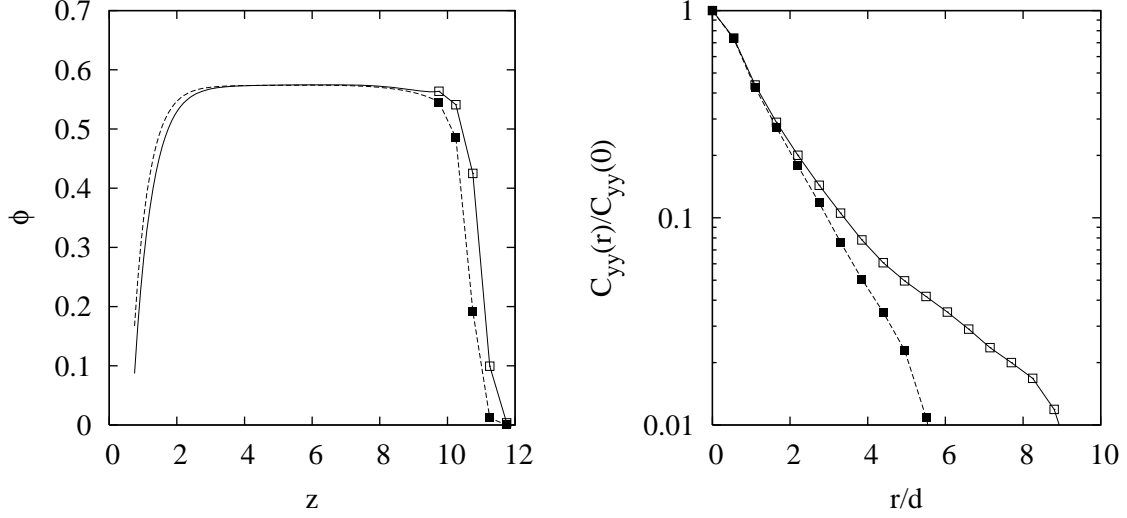


FIG. 14: Volume fraction profiles (time-averaged and smoothed) (a) and velocity correlation functions (b) for $20d \times 20d$ (\square) and $40d \times 40d$ (\blacksquare) base area with $h/d \simeq 10$, $\theta = 23^\circ$, $\Delta t/\tau_0 = 1$.

larger. The first four points in correlation function are, however, the same. This justifies our method of obtaining λ_{yy} by fitting the exponential decay function to the first four points of correlation data.

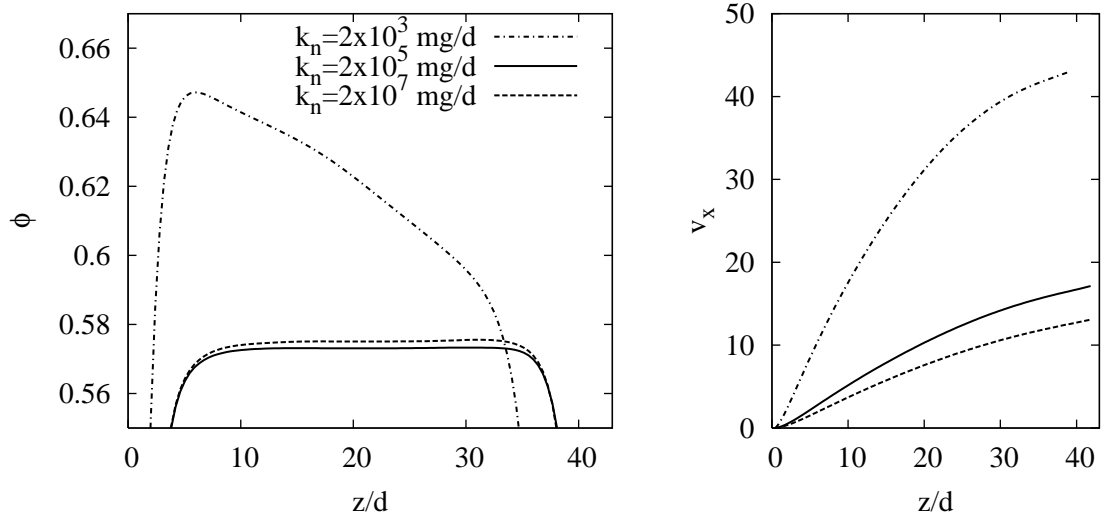


FIG. 15: (a) Volume fraction profiles for different values of grain stiffness (data smoothing routine used in addition to time averaging). $h/d \simeq 40$ and $\theta = 23^\circ$. (b) Velocity profiles for the same configurations shown in (a).

To study the dependence on spring stiffness k_n , we carried out simulations for the tall

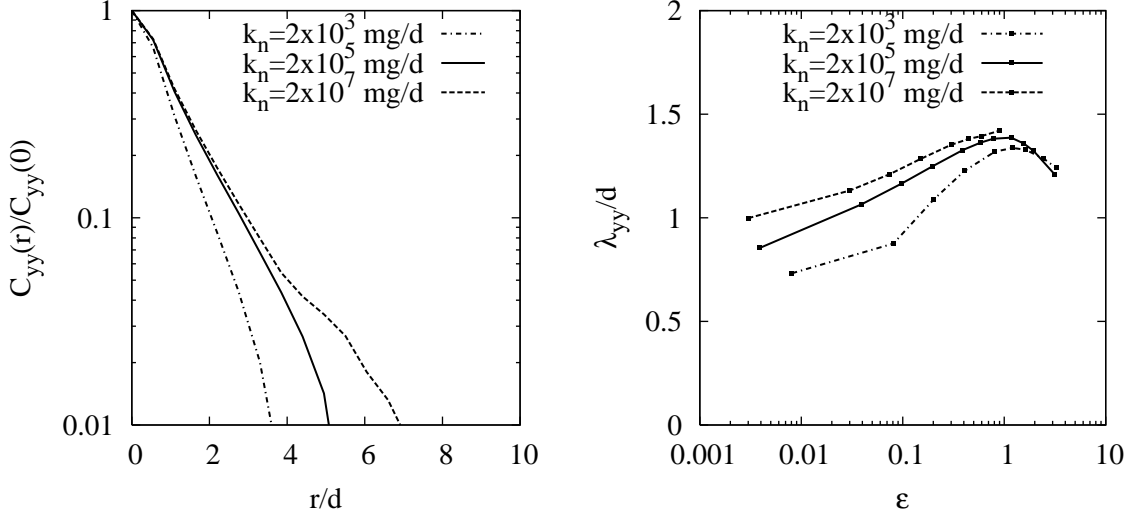


FIG. 16: (a) Velocity correlation function at $\epsilon \simeq 0.1$ and (b) correlation lengths for three values of grain stiffness. $h/d \simeq 40$ and $\theta = 23^\circ$.

pile $h/d \simeq 40$ at $\theta = 23^\circ$ with $k_n = 2 \times 10^3$ mg/d and $k_n = 2 \times 10^7$ mg/d and compared the results with earlier $k_n = 2 \times 10^5$ mg/d results. Changes of stiffness affect the collision time and restitution coefficients and require appropriate adjustments of the timestep and viscoelastic parameter [2]. Therefore, for the case of increased stiffness, $k_n = 2 \times 10^7$ mg/d, the timestep was decreased to $\delta t/\tau_0 = 10^{-5}$ and γ_n was set to $\gamma_n = 500 \sqrt{g/d}$. In the case of the soft material, $k_n = 2 \times 10^3$ mg/d, the timestep was kept at the same typical value, $\delta t/\tau_0 = 10^{-4}$, and the viscoelastic dumping constant was reduced to $\gamma_n = 5 \sqrt{g/d}$.

Figure 15(a) shows that increasing the stiffness by two orders of magnitude increases the value of bulk volume fraction from 0.573 to only 0.575. The stiffer grains flow with slightly lower velocities, Fig. 15(b). Decreasing the stiffness by two orders of magnitude has a big qualitative effect. The bulk is no longer characterized by a constant volume fraction. The grains closer to the bottom are compressed by the weight of the system, leading to a decreasing with depth volume fraction profile. Figure 16(a) shows the effect of the coefficient of stiffness on the two-point correlations function $C_{yy}(r)$, measured at $\Delta t/\tau_0 = 0.1$ for soft grains and $\Delta t/\tau_0 = 0.25$ for typical and stiff grains. This choice of Δt provides approximately equal value of measurement strain, $\epsilon \simeq 0.1$. Again, we note a negligibly small difference between the results with typical and stiff grains. The results for soft grains indicate a smaller correlation length. The difference between correlation length for the three configurations is

small and decreases with the increase of ϵ , see Fig. 16(b). In summary, the effect of variations in k_n is minimal as long as $k_n \geq 2 \times 10^5 \text{ mg}/d$.

-
- [1] P. Jop, Y. Forterre, and O. Pouliquen, *Nature* **441**, 727 (2006).
 - [2] L. E. Silbert, D. Ertas, G. S. Grest, T. C. Halsey, D. Levine, and S. J. Plimpton, *Phys. Rev. E* **64**, 051302 (2001).
 - [3] P.-A. Lemieux and D. J. Durian, *Phys. Rev. Lett.* **85**, 4273 (2000).
 - [4] E. Azanza, F. Chevoir, and P. Moucheron, *J. Fluid. Mech.* **400**, 199 (1999).
 - [5] O. Pouliquen, *Phys. Fluids* **11**, 542 (1999).
 - [6] D. Ertas and T. C. Halsey, *Europhys. Lett.* **60**, 931 (2002).
 - [7] G. D. R. MiDi, *Euro. Phys. J. E* **14**, 341 (2004).
 - [8] F. da Cruz, S. Emam, M. Prochnow, J.-N. Roux, and F. Chevoir, *Phys. Rev. E* **72**, 021309 (2005).
 - [9] O. Pouliquen, *Phys. Rev. Lett.* **93**, 248001 (2004).
 - [10] L. E. Silbert, *Phys. Rev. Lett.* **94**, 098002 (2005).
 - [11] N. Taberlet, P. Richard, A. Valance, W. Losert, J. M. Pasini, J. T. Jenkins, and R. Delannay, *Phys. Rev. Lett.* **91**, 264301 (2003).
 - [12] L. E. Silbert, J. W. Landry, and G. S. Grest, *Phys. Fluids* **15**, 1 (2003).
 - [13] L. Berthier, G. Biroli, J.-P. Bouchaud, L. Cipelletti, D. E. Masri, D. L'Hote, F. Ladieu, and M. Pierno, *Science* **310**, 1797 (2005).
 - [14] D. Ertas and T. C. Halsey, in preparation for publication.
 - [15] The contact stiffness is related to the Young's modulus E and Poisson ratio ν of the spheres through $k_n = \frac{Ed}{3(1-\nu^2)}$. The typical value of stiffness $k_n = 2 \times 10^5 \text{ mg}/d$ used in our simulations corresponds approximately to the behavior of 1 cm diameter rubber balls. As is shown in previous simulations [2] and in Appendix B, increasing k_n does not change any result qualitatively.